# Effects of Isothermal Aging on the Microstructure Evolution and Pitting Corrosion Resistance of Lean Duplex Stainless Steel UNS S32003

LIANG HE, LOVELYN WIRIAN, and PREET M. SINGH

UNS S32003 materials were aged at temperatures in the range of 873 K to 1173 K (600 °C to 900 °C) for 30 minutes and 2 hours. Nitrides were found to precipitate along the ferrite/austenite phase boundaries and within the ferrite phase. The precipitation kinetics was the fastest at 1073 K (800 °C), at which temperature the Cr-depleted zones were observed to be in the vicinity of the precipitates. Precipitation and resultant Cr-depleted zone led to the highest pitting susceptibility of the UNS S32003, aged at 1073 K (800 °C), when tested in 0.6 mol/L NaCl solution. To observe the precipitation evolution, the UNS S32003 specimens were aged at 973 K (700 °C) for different time periods for up to 120 hours. Within aging time up to 24 hours at 973 K (700 °C), only nitrides precipitates were observed and an intermetallic phase was observed after 120 hours of aging along with an increase in the percentage of precipitates. Pitting potential dropped with increasing aging time and metastable pitting rate increased with longer aging time period, both indicating a negative effect of aging on pitting corrosion resistance of the lean duplex stainless steel UNS S32003.

## I. INTRODUCTION

DUPLEX stainless steels (DSSs) are alloys that contain both ferrite phase and austenite phase in the microstructure with an optimum volume ratio of 50:50. The ferrite phase has body-centered cubic (BCC) crystal structure, while the austenite phase has a face-centered cubic (FCC) crystal structure. The ferrite phase has high tensile strength and fatigue strength and the austenite phase provides good formability and high toughness. The combination of the two phases gives the DSSs both high mechanical strength and excellent corrosion and stress corrosion cracking resistance compared with austenitic and ferritic stainless steels. Because of these features, DSSs have wide applications in the pulp and paper industry, chemical process industry, oil and gas industry, pharmaceutical industry, and as structural materials.

As mentioned above, the optimum performance of DSSs is achieved when the ferrite phase and austenite phase are balanced. However, processes such as welding,[1–4] annealing treatment[5–7] as well as aging[8–17] can change the ferrite-to-austenite ratio, phase composition or lead to the formation of secondary phases including intermetallic phases or carbide and nitride precipitates, and thus further change the performance of duplex stainless steels. Precipitation of $\sigma$ phase and $\chi$ phase in standard UNS S31803 (DSS 2205) and super DSSs has been widely investigated.[8–14] Both $\sigma$ phase and $\chi$ phase are Cr and Mo enriched, but the Cr content is higher in $\sigma$ phase than that in $\chi$ phase while the Mo content is higher in $\chi$ phase.[8–10] $\sigma$ phase forms within the temperature range of around 923 K to 1173 K (650 °C to 900 °C). In the DSS 2205 as well as in super DSSs, it is precipitated within minutes of aging at the ferrite/austenite boundaries and grows into the ferrite phase because of the high content of Cr and Mo and higher diffusion rate in the ferrite phase.[9,12,13]

Different from the fast formation of $\sigma$ phase and $\chi$ phase in standard and super DSSs, the precipitation of intermetallic phases is sluggish in the lower-alloyed lean duplex stainless steels (LDSSs) UNS S32101 and UNS S32304 because of their reduced Cr and Mo content. $Cr_2N$ and $M_{23}C_6$ were found to precipitate after minutes of aging in LDSS 2101 along the ferrite/austenite interface and the ferrite/ferrite boundaries while the $\sigma$ phase were detected after 24 hours of aging at 963 K (690 °C).[15] The nucleation and growth of precipitates and intermetallic phases at the ferrite/austenite boundaries also leads to the formation of the secondary austenite in the ferrite phase, which is depleted in Cr and

LIANG HE, LOVELYN WIRIAN, and PREET M. SINGH are with the School of Materials Science and Engineering, Georgia Institute of Technology, Atlanta, GA 30318. Contact e-mail: preet.singh@mse.gatech.edu

Mo.[8,15] $Cr_2N$ can also precipitate within the ferrite phase during fast cooling from high annealing temperature when N is saturated in the ferrite phase and as the diffusion to the austenite phase is not fast enough.[16]

The precipitation of secondary phases leads to the deterioration of both corrosion resistance and mechanical properties of DSSs.[13,14,16,18–22] Corrosion resistance of DSSs has been found to decrease with aging times where the depleted zones in the vicinity of precipitates are the most susceptible sites for pitting corrosion initiation. Li *et al.* used a potentiostatic polarization method to measure the critical pitting temperature (CPT) of the aged DSSs specimens in NaCl solution and reported that the CPT drop is sensitive to the microstructure evolution at the short aging time.[18–21] The breakdown potential and CPT can reveal the pitting corrosion resistance of the most susceptible sites in the microstructure, Wilms used the critical current density during potentiodynamic polarization in simulated crevice solution as an indication of the general surface deterioration of super duplex stainless steels during aging.[13] While large drop in the pitting corrosion resistance occurs in aged DSSs specimens in chloride-containing environment, it is not observed in aged UNS S32101 specimens in caustic environments, although the precipitates and the depleted areas are present in the microstructure.[23]

In this study, the effects of aging treatment on the microstructure change and pitting corrosion behavior of newly developed lean duplex stainless steel UNS S32003 were studied. Aging treatments were performed at temperatures in the range of 873 K to 1173 K (600 °C to 900 °C) for up to 2 hours. The materials were also aged at 973 K (700 °C) for different time periods to study the microstructural evolution over longer times. The samples were tested in 0.6 mol/L NaCl solution at 323 K (50 °C) through potentiodynamic cyclic polarization to compare their pitting corrosion susceptibility.

## II. EXPERIMENTS

### A. *Materials and Heat-Treatment Conditions*

The material used in this study was a lean duplex stainless steel UNS S32003 and its chemical composition is shown in Table I. The materials were cut into $10 \times 10 \times 3$ mm$^3$ pieces for heat-treatment. The specimens were first annealed at 1313 K (1040 °C) in a pre-heated furnace for one hour and then water quenched. To study the phase transformation at different temperatures, the specimens were aged at temperatures within the range of 873 K to 1173 K (600 °C to 900 °C) with 50 K (50 °C) intervals for 30 minutes and 2 hours in furnace, respectively, followed by water quenching to preserve the microstructure formed after that aging treatment. To observe the evolution of microstructure over aging time, the specimens were aged at 973 K (700 °C) for different time periods from 10 minutes up to 120 hours.

### B. *Corrosion Tests*

For corrosion test samples, a metal wire was attached at the back of the heat-treated specimens to ensure electric connection and the specimens were then mounted in epoxy. The surface of the mounted samples was ground to 2000 grit and ultrasonically cleaned in acetone before each test. The interface between the specimen and the epoxy was covered by an electroplating tape with a hole to avoid the crevice corrosion and to expose the same surface area of 0.6 cm$^2$ for each test.

Potentiodynamic cyclic polarization tests were done in deaerated 0.6 mol/L NaCl solution at 323 K (50 °C) to compare the pitting corrosion resistance of differently heat-treated samples. The test solution was prepared from analytical grade reagents and deionized water. The test cell was three-electrode system with Pt foil as the counter electrode and a saturated calomel electrode (SCE) as the reference electrode. All potentials mentioned here are with respect to SCE and denoted as $V_{SCE}$. The surface was first conditioned at $-0.8$ $V_{SCE}$ for 20 minutes to remove the native oxide film formed in air, and then the open circuit potential (OCP) was measured for 1 hour. Then, the potential was swept from 100 mV below the OCP to 1.2 $V_{SCE}$ or until a current density of 0.2 mA/cm$^2$ was reached. The forward scan rate was 1mV/s and the reverse scan rate was 5 mV/s. The reverse scan rate was five times faster than the forward scan rate to avoid the overgrowth of pits. Any data, where the sample showed signs of crevice corrosion after the test, was discarded. At least three polarization tests were conducted to ensure the reproducibility of data. In subsequent analysis of data, pitting potential ($E_{pit}$) was defined as the potential at which the current density exceeded 100 $\mu$A/cm$^2$ and the repassivation potential ($E_{rp}$) was defined as the potential where the backward scan curve intersected the forward scan curve, as shown in Figure 1.

Metastable pitting events were also studied for the samples aged at 973 K (700 °C) for different time periods. The current peaks during the forward scan before stable pitting represented the abrupt current increase followed by the repassivation of metastable pitting events. The numbers of peaks within every 100 mV intervals were counted after each test. The rate of occurrence of metastable pitting was defined as the number of metastable pitting events divided by the time period, which in this case is 100 seconds for 100 mV interval with 1 mV/s forward scan rate.

### C. *Material Characterization*

To characterize the proportion of the ferrite phase and the austenite phase in samples annealed at 1313 K (1040 °C), optical microscope was used. The sample was ground and polished to mirror finish using 0.05 $\mu$m alumina and then electrolytically etched in 40 wt pct NaOH at 2.5 V. The volume fraction of the ferrite phase was quantified using point-counting method. Ten different field of views were analyzed. In addition, the ferrite number of the annealed sample was measured using a Feritscope.

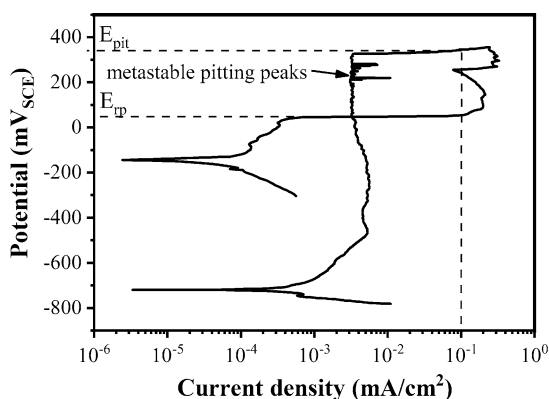| Table I. | Chemical Composition of UNS S32003 | | | | | | | | | |
|---|---|---|---|---|---|---|---|---|---|---|
| Element | Cr | Ni | Mo | Mn | Cu | C | P | S | N | Si |
| Wt Pct | 21.7 | 4.0 | 1.64 | 1.72 | 0.17 | 0.015 | 0.025 | ≤ 0.001 | 0.17 | 0.32 |



Fig. 1—Typical cyclic potentiodynamic polarization curve of aged sample in 0.6 mol/L NaCl solution at 50 °C.

Scanning electron microscopy (SEM, Hitachi 8230) coupled with the energy-dispersive X-ray spectroscopy (EDS, Oxford Instrument AZtec®) was used to characterize the microstructure and composition of different phases in the heat-treated samples. The samples were ground and then polished to mirror finish using 0.05 $\mu$m alumina. Two different etchants were used in this study. Electrolytic etching in 40 wt pct NaOH etchant at 2.5 V was used to create better phase contrast for image analysis, but this method tends to etch out the precipitates. Chemical etching in Pellegrino's etchant, consisting of 25 mL nitric acid, 50 mL hydrochloric acid and 50 mL distilled water, has a slow etching rate and was used for positive identification of secondary phases.

To identify and confirm the phases present in the heat-treated samples, X-ray diffraction (XRD) characterization was carried out with Cu $K_{\alpha 1}$ radiation with a wavelength of 0.15406 nm. The diffraction angle ($2\theta$) was in the range of 35 through 60 deg. The scan step was 0.033 deg and the time per step was 350 seconds.

To study the pit initiation sites, the samples were first polished to mirror finish using 0.05 $\mu$m alumina and etched in Pellegrino's etchant, and then potentiostatically polarized at 800 $mV_{SCE}$ in 0.6 mol/L NaCl at 323 K (50 °C) to induce pit initiation. Since the secondary phases remained after etching, it can be confirmed that the pits produced were not etch pits. The pit nucleation locations were then characterized using SEM.

## III. RESULTS

Figure 2 shows one typical optical micrograph of the sample annealed at 1313 K (1040 °C). The average volume fraction of the ferrite phase in the annealed sample was 50.1 pct with a 95 pct confidence interval
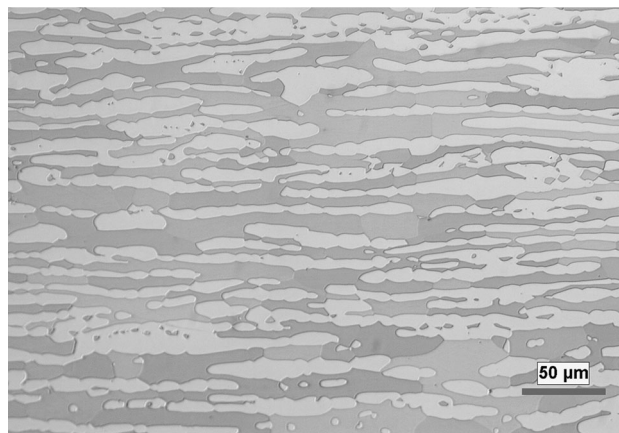


Fig. 2—Optical micrograph showing the microstructure of the sample annealed at 1313 K (1040 °C).

(CI) of 2.7 pct. The average ferrite number (FN) of the annealed sample was 54.0 with a 95 pct CI of 2.9. The ferrite phase is balanced with the austenite phase in UNS S32003 specimen when it is annealed at 1313 K (1040 °C).

### A. Effects of Aging Temperature on Microstructure Evolution

The microstructure of samples aged at different temperatures, from 873 K to 1173 K (600 °C to 900 °C), for 2 hours, is shown in Figure 3. Since the polished sample surface was etched in NaOH solution, the dark phase represents the ferrite phase, and the light phase is the austenite phase. The black spots are precipitates and they form mainly along the ferrite/austenite phase boundaries as well as within the ferrite phase. At 873 K (600 °C), the precipitates can rarely be observed, indicating a very slow precipitation kinetics at 873 K (600 °C). The precipitates formed after 2 hours of aging at 973 K to 1173 K (700 °C to 900 °C) and the amount of precipitates reached maximum at 1073 K (800 °C). This was confirmed by image analysis, which calculated the volume fraction of the precipitates, as shown in Figure 4.

To positively identify the chemical composition of each phase, Pellegrino's etchant was used to preserve the precipitates. Figure 5 shows the microstructure of a sample aged at 1123 K (850 °C) for 2 hours and the chemical composition of each phase was characterized by EDS analysis, the results of which are shown in Table II. Compared to the bulk phase, the precipitates are enriched in Cr and N, confirming that these precipitates are nitrides. It should be noted that EDS analysis of elements with light atomic weight (nitrogen
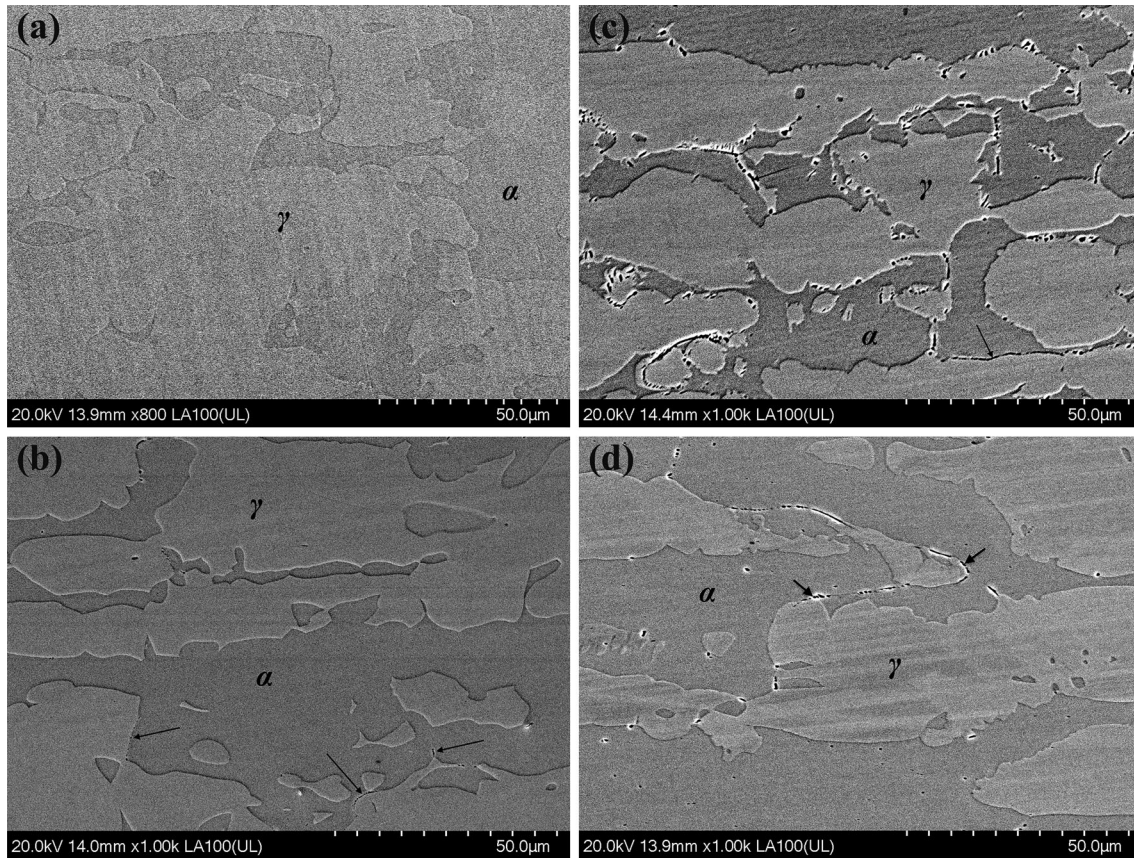
Fig. 3—SEM images of the NaOH-etched microstructure of samples aged at (*a*) 873 K (600 °C); (*b*) 973 K (700 °C); (*c*) 1073 K (800 °C); (*d*) 1173 K (900 °C) for 2 h. Black arrows indicate the location of precipitates.
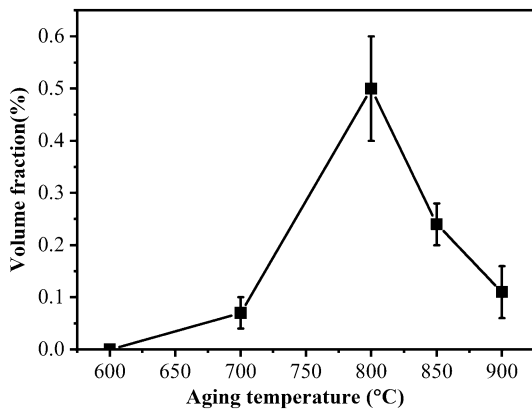


Fig. 4—Change in the volume fraction of precipitates with different aging temperature for 2 h.
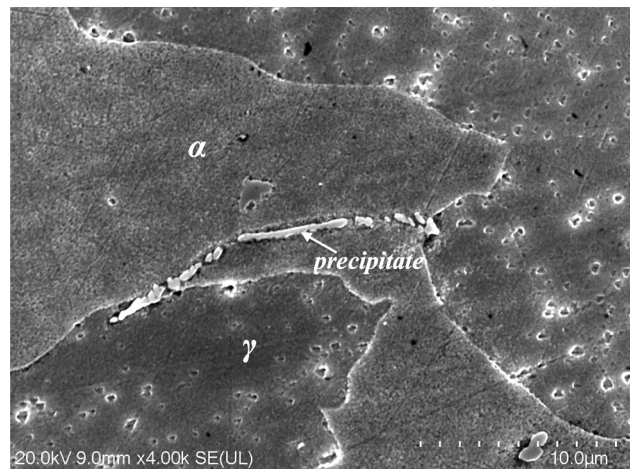


Fig. 5—Secondary electron (SE)-SEM image of the microstructure of sample aged at 1123 K (850 °C) for 2 h. The polished surface was etched by Pellegrino's etchant.

in this case) is semi-quantitative, however, the contents of nitrogen in different phases can still be compared qualitatively using EDS.

Because of the enrichment of Cr content in the precipitates, the areas surrounding the precipitates are often depleted in Cr. EDS line scan was performed across the precipitates formed in samples aged at 1073 K and 1173 K (800 °C and 900 °C) for 2 hours to identify if there is an existence of depleted zones, as

shown in Figures 6 and 7. Figure 6(b) shows the Cr, Fe, Ni and Mn profiles across the precipitates formed along the ferrite/austenite boundary in a sample aged at 1073 K (800 °C) for 2 hours. The line-scan started from the ferrite phase and ended within the austenite phase. The Cr-depleted zones formed next to the precipitates

**Table II.  Chemical Composition of the Ferrite Phase, Austenite Phase and Precipitates in Sample Aged at 1123 K (850 °C) for 2 h**

|     | Ferrite | Austenite | Precipitates |
| --- | --- | --- | --- |
| Cr | 23.6 ± 1.1 | 19.8 ± 0.7 | 27.6 ± 2.8 |
| Ni | 2.3 ± 0.1 | 4.6 ± 0.4 | 3.1 ± 0.6 |
| Mo | 1.7 ± 0.4 | 1.1 ± 0.2 | 0.9 ± 0.4 |
| Mn | 1.6 ± 0.1 | 1.9 ± 0.1 | 1.2 ± 0.2 |
| N | — | 0.1 ± 0.1 | 4.5 ± 1.2 |

and on the side of the ferrite phase. The Cr content in the depleted zone was lower than that for both the ferrite phase and the austenite phase. In comparison, the line-scan of Fe showed that the content of Fe was higher in the Cr-depleted zone compared with that in the ferrite phase and was decreased in the nitride precipitate. The counts of Ni and Mn were low and their content changes were less remarkable. Cr-depleted zones also formed near the precipitates in the ferrite phase, as shown in Figure 6(c). There was also enrichment of Fe and Ni in the Cr-depleted zones. The chemical composition of the
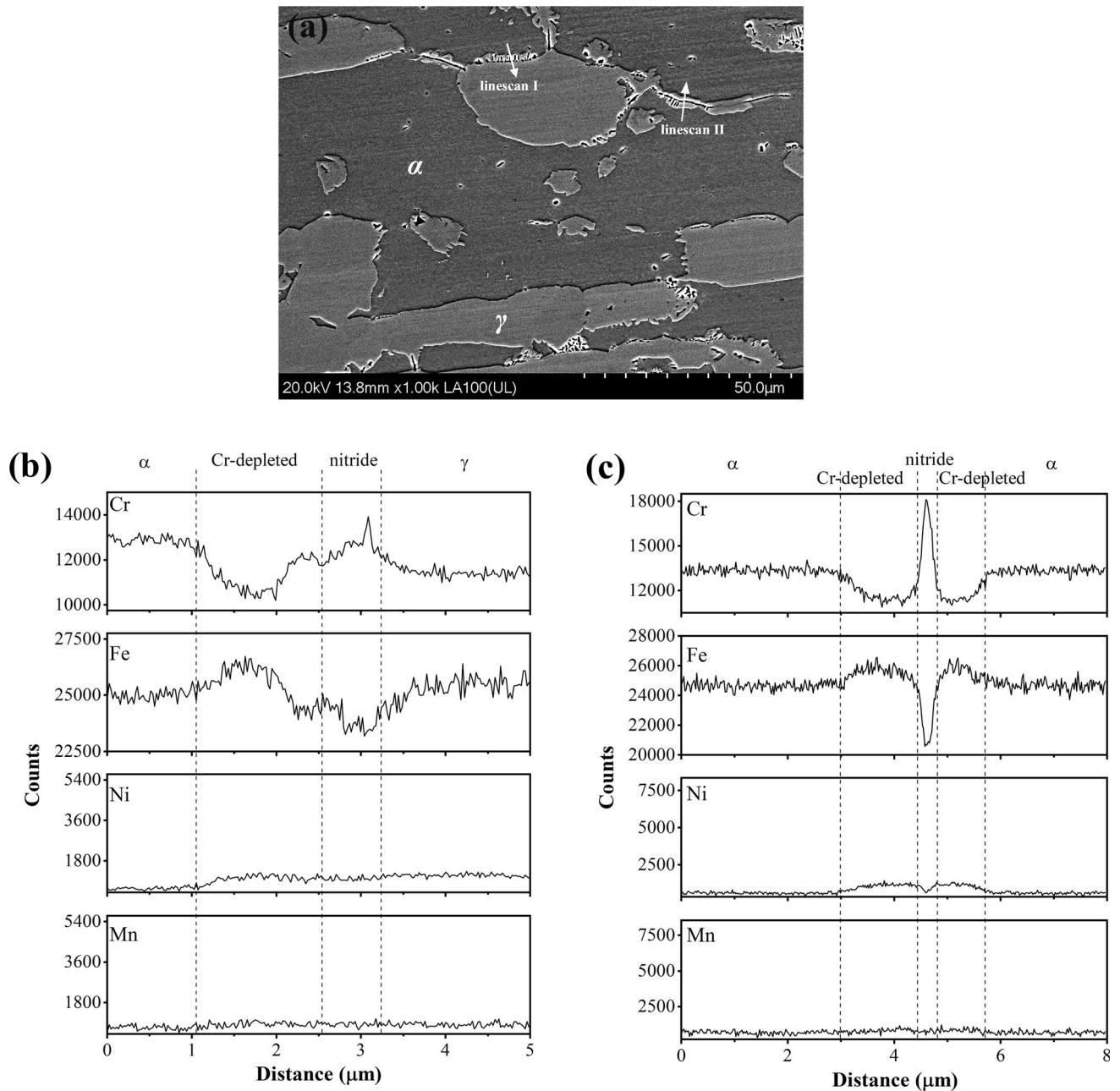


Fig. 6—Line-scans across precipitates formed in samples aged at 1073 K (800 °C) for 2 h. (*a*) SEM image showing the location of different linescans; (*b*) K series line-scan I of Cr, Fe, Ni and Mn across precipitates formed at the ferrite/austenite phase boundaries; (*c*) K series line-scan II of Cr, Fe, Ni and Mn across precipitates formed within the ferrite phase.
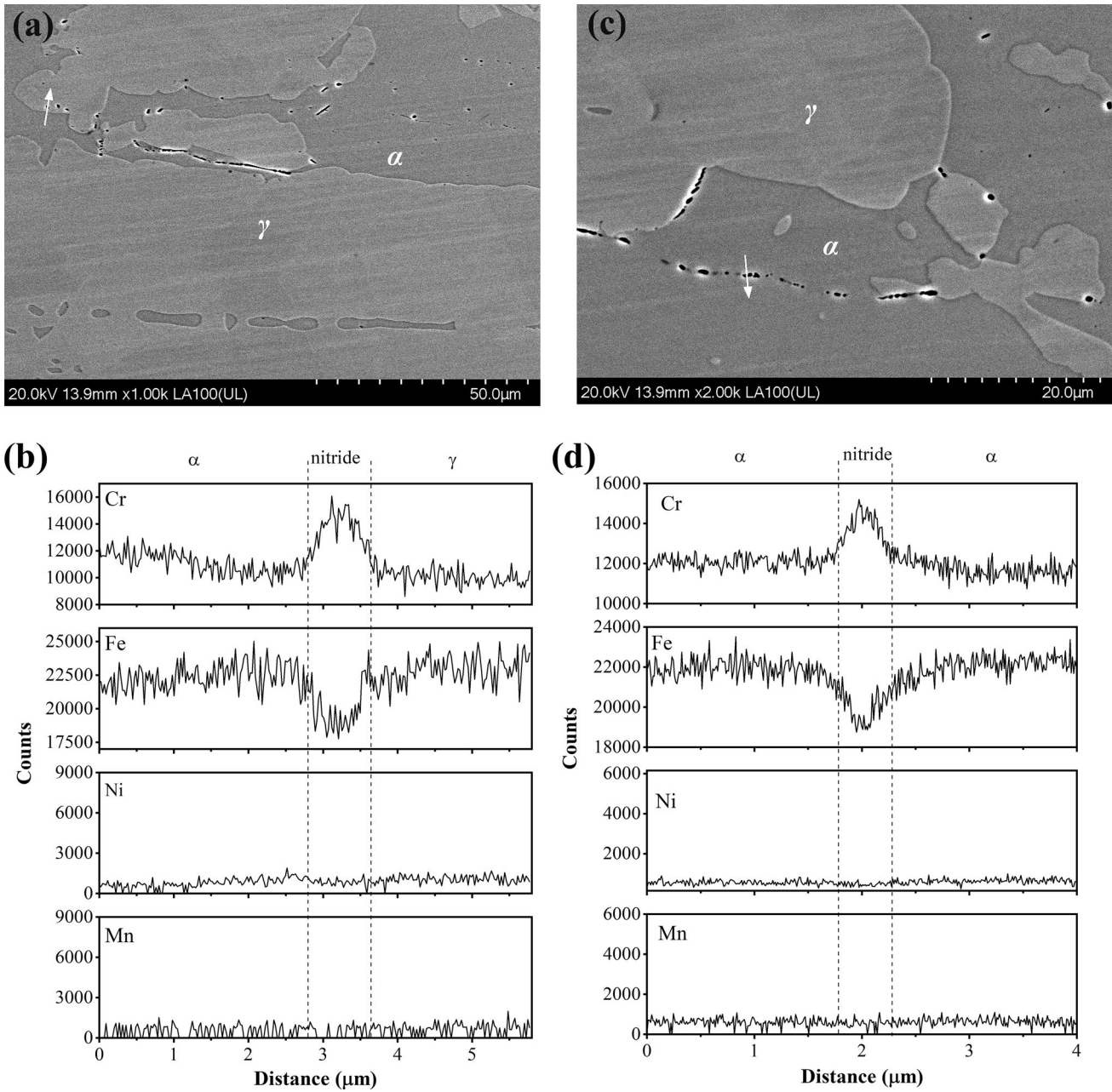
Fig. 7—Line-scans across precipitates formed in a sample aged at 1173 K (900 °C) for 2 h. (*a*) SEM image showing line-scan across precipitates formed along ferrite/austenite boundaries; (*b*) K series-line-scans of Cr, Fe, Ni and Mn across precipitates along ferrite/austenite phase boundaries; (*c*) SEM image showing line-scan across precipitates formed within the ferrite phase; (*d*) K series-line-scans of Cr, Fe, Ni and Mn across precipitates within the ferrite phase.

**Table III. Comparison Between the Amount of Major Elements in the Ferrite Phase, Austenite Phase, and Depleted Zones in Samples Aged at 1073 K (800 °C) for 2 h**

|     | Ferrite        | Austenite      | Depleted Zones |
| --- | -------------- | -------------- | -------------- |
| Cr  | 24.1 ± 0.6     | 20.8 ± 0.4     | 18.4 ± 0.1     |
| Ni  | 2.6 ± 0.2      | 4.7 ± 0.1      | 4.9 ± 0.1      |
| Mo  | 1.9 ± 0.2      | 1.1 ± 0.1      | 1.1 ± 0.1      |
| Mn  | 1.6 ± 0.1      | 1.9 ± 0        | 2.1 ± 0.1      |
| N   | 0.1 ± 0.1      | 0.2 ± 0.2      | 0.4 ± 0.1      |

depleted zones was compared with that of the bulk phases and was summarized in Table III.

However, for the sample aged at 1173 K (900 °C) for 2 hours, no distinct Cr-depleted areas were observed from SEM images close to the precipitates shown in Figures 7(a) and (c). Similar line-scans were performed across the precipitates, but the Cr content next to the precipitates along ferrite/austenite boundaries was similar as that for the austenite phase, and there was no depletion of Cr positively detected at both sides of precipitates formed in the ferrite phase, as shown in Figures 7(b) and (d), respectively.

### B. Pitting Corrosion Behavior of Samples Aged at Different Temperatures

The samples aged at different temperatures were tested in 0.6 mol/L NaCl at 50 °C to compare their pitting corrosion susceptibility. The pitting potential, $E_{pit}$, of different samples was acquired after each corrosion tests and compared, as shown in Figure 8. Pitting potential vs. aging temperatures curve showed a V shape, where the pitting potential first decreased from aging temperature of 923 K (650 °C) and then reached a minimum for samples aged at 1073 K to 1123 K (800 °C to 850 °C). The pitting potential then increased again for the samples aged at temperature of 1173 K (900 °C), but it was lower than that for the samples aged at 973 K (700 °C), as shown in Figure 8.

To identify the pit initiation site, very small pits were initiated on the polished and etched surface potentiostatically. Pit initiation site is shown in Figure 9. A small pit with diameter of around 3 $\mu$m is located at the ferrite/austenite boundary, and close to the precipitates. The location of pit initiation site is similar to where the depleted zones are located.

### C. Effects of Aging Time on Microstructure Evolution

To observe the microstructure evolution over time, the samples were aged at 973 K (700 °C) for different time periods from 10 minutes up to 120 hours. For samples aged at 973 K (700 °C) for 2 hours and 24 hours, only nitride precipitates were observed, which appeared as dark spots in the NaOH-etched microstructure as shown in Figures 10(a) and (b). The volume fraction of precipitates increased from 0.07 to 0.41 pct. To reveal the detailed morphology of precipitates, high-magnification SEM images were taken on surfaces of samples etched in Pellegrino's etchant, as shown in Figures 11(a) and (b). EDS analysis also confirmed that the area in the vicinity of precipitates was depleted in Cr in the sample aged at 973 K (700 °C) for 24 hours.

Figures 10(c) and 11(c) show the microstructure of samples aged at 973 K (700 °C) for 120 hours and etched in NaOH and Pellegrino's etchant. The surface

fraction of the precipitates further increased to 0.97 pct. However, along with the formation of precipitates, intermetallic phase with larger size than the precipitates was also observed along the ferrite/austenite boundaries and within the ferrite phase in the sample aged for 120 hours. The chemical composition of intermetallic phases is shown in Table IV. The intermetallic phases are enriched in Cr and Mo and the Mo content is quite consistent with a value of around 4.6 wt pct, confirming they are $\sigma$ phase.

In addition to SEM/EDS analysis to characterize the microstructure of heat-treated samples, X-ray diffraction (XRD) was also carried out on the annealed sample and two samples aged at 973 K (700 °C) to identify the phases present in the heat-treated specimens. Figure 12(a) shows the XRD pattern of the specimen annealed at 1313 K (1040 °C) and only diffraction peaks of the ferrite phase and the austenite phase were identified. Similar to the XRD pattern of the annealed specimen, the diffraction pattern of the specimen aged at 973 K (700 °C) for 24 hours only showed the peaks of the ferrite phase and the austenite phase and no nitride peaks showed up, although SEM images in Figures 10(b) and 11(b) showed the presence of nitride precipitates. This is probably due to the low fraction (0.41 pct) of nitrides formed in the specimen aged at 973 K (700 °C) for 24 hours.

In comparison, in the XRD pattern of the specimen aged at 973 K (700 °C) for 120 hours, in addition to the ferrite and austenite peaks, diffraction peaks of the $\sigma$ phase were present. $\chi$ phase (331) diffraction peak was labeled in Figure 12(c) because it overlapped with $\sigma$ (331) peak. However, this may not indicate that $\chi$ phase was present in the specimen aged at 973 K (700 °C) for 120 hours. It has been demonstrated that SEM coupled with EDS analysis is more powerful to predict the existence of $\chi$ phase because of the overlapping of XRD peaks of $\chi$ phase with XRD peaks of other phases.[8] Since $\chi$ phase was not positively identified in SEM/EDS analysis, it strongly indicates that $\chi$ phase was not present in the microstructure of the specimen aged at
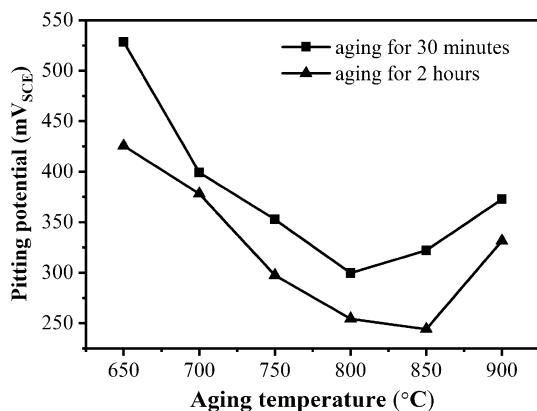


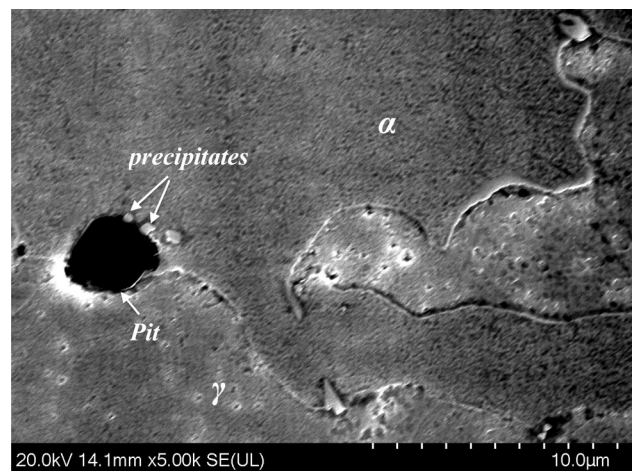Fig. 8—Change of pitting potential with different aging temperatures for two different times.



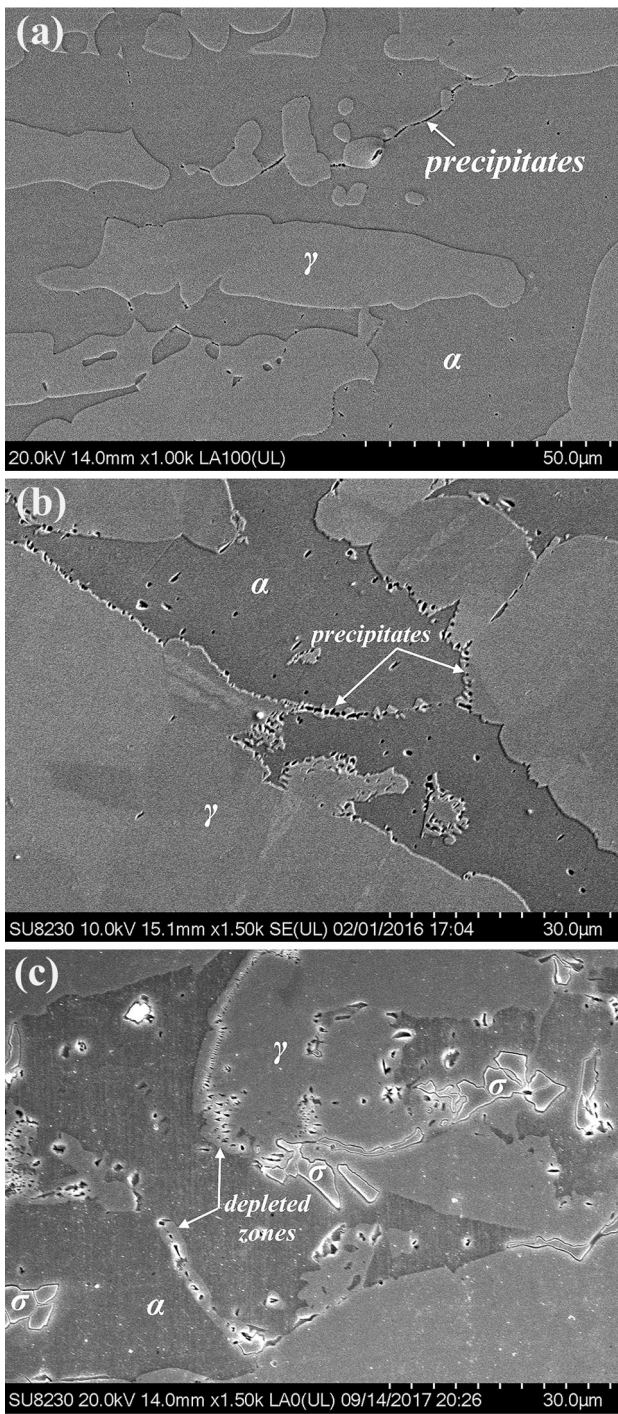Fig. 9—SE-SEM image showing the pit initiation site in the vicinity of precipitates.

Fig. 10—SEM images of samples aged at 973 K (700 °C) for (*a*) 2 h; (*b*) 24 h; (*c*) 120 h. Sample surface was etched in 40 pct NaOH etchant.



Fig. 11—SEM images of microstructure of samples aged at 973 K (700 °C) for (*a*) 5 h; (*b*) 24 h; (*c*) 120 h.

973 K (700 °C) for 120 hours. In comparison, while there was no diffraction peaks of nitride precipitates, SEM images in Figures 10(c) and 11(c) showed the presence of nitride precipitates but in very low amount (0.97 pct), and therefore, the diffraction peaks of nitrides did not show up in the XRD pattern.

### D. *Pitting Corrosion Resistance of Samples Aged at 973 K (700 °C) for Different Aging Time*

Pitting corrosion behavior of samples aged at 973 K (700 °C) for different time period was tested in 0.6 mol/L NaCl solution at 323 K (50 °C). The pitting potential and the repassivation potential dropped with longer aging time, as shown in Figure 13, indicating an increasing pitting corrosion susceptibility over time.

**Table IV.  EDS Analysis of Chemical Composition of Samples Aged at 700 °C for 120 h**
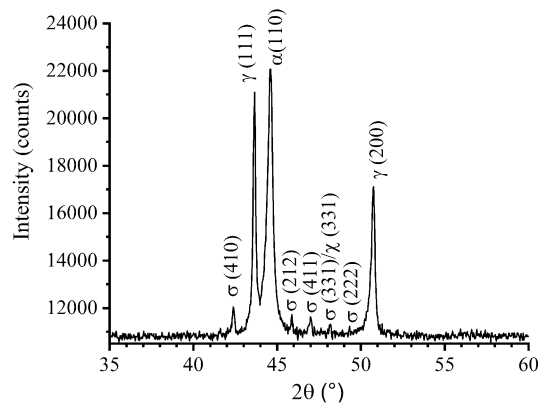
|  | Ferrite | Austenite | $\sigma$ Phase | Depleted zones |
|---|---|---|---|---|
| Cr | 23.0 ± 0.3 | 20.0 ± 0.1 | 28.5 ± 1.9 | 18.4 ± 0.1 |
| Ni | 2.0 ± 0.2 | 4.6 ± 0.0 | 2.1 ± 0.2 | 4.9 ± 0.1 |
| Mo | 1.5 ± 0.3 | 1.0 ± 0.2 | 4.6 ± 0.4 | 1.1 ± 0.1 |
| Mn | 1.5 ± 0.1 | 1.9 ± 0.0 | 1.8 ± 0.1 | 2.1 ± 0.1 |
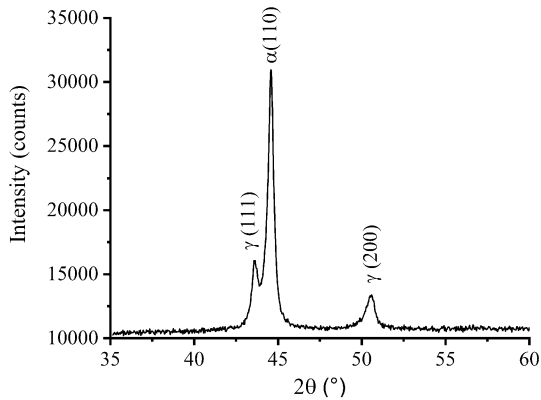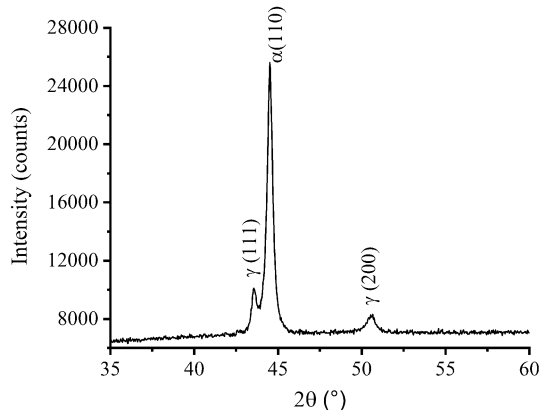


Fig. 12—XRD patterns of samples (*a*) annealed at 1313 K (1040 °C) for 1 h; (*b*) aged at 973 K (700 °C) for 24 h; and (*c*) aged at 973 K (700 °C) for 120 h.
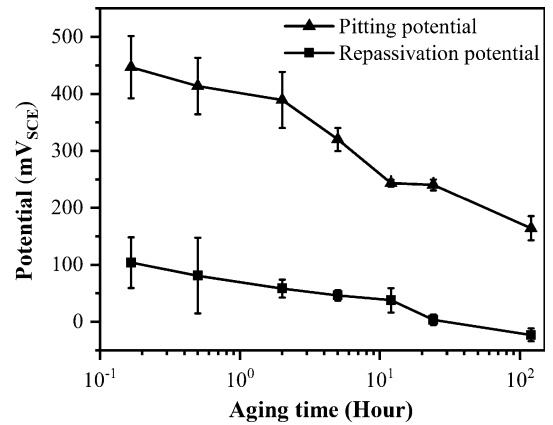


Fig. 13—Change in pitting potential and repassivation potential with aging time at 973 K (700 °C).

The deviation of pitting potential is large for the samples aged for shorter periods of time up to 5 hours.

The approach used to study the effect of aging temperature on pitting corrosion behavior was also used to study the pit initiation site in samples aged at 973 K (700 °C). Similar to the small pit observed in the sample aged at 1123 K (850 °C) for 2 hours, the small pit initiated in the sample aged at 973 K (700 °C) for 24 hours is also located at the ferrite/austenite boundary with nitride precipitation (Figure 14).

Rate of metastable pitting in samples aged at 973 K (700 °C) for different time periods was calculated and shown in Figure 15. Only metastable pitting rate in the potential range of 0 through 100 $mV_{SCE}$ and 100 through 200 $mV_{SCE}$ was compared since above 200 $mV_{SCE,}$ stable pits would develop in the samples aged for 120 hours. Higher rate of metastable pitting indicates a higher frequency of film breakdown and repassivation, which is also an indication of higher pitting corrosion susceptibility. The rate of occurrence of metastable pitting within the potential range of 0 through 100 mV and 100 through 200 mV increased with the longer aging time period, indicating that the aging for longer time periods deteriorate pitting corrosion resistance of UNS S32003.

## IV.  DISCUSSIONS

### A. *Phase Transformation*

After an isothermal aging of UNS S32003 within the temperature range of 873 K to 1173 K (600 °C to 900 °C) for 2 hours, only nitride precipitates were positively identified while the intermetallic phases were not detected, as shown in Figures 3 and 5. Similar phenomena has been reported for duplex stainless steels UNS S32101 and S32304 that also have leaner alloying content, especially lower Mo content, and only nitrides and carbides were detected after hours of aging in the temperature range of 973 K to 1123 K (700 °C to 850 °C).[17,24,25] However, for standard S32205 and super DSSs, intermetallic phases form within minutes when aged at 1073 K or 1123 K (800 °C or
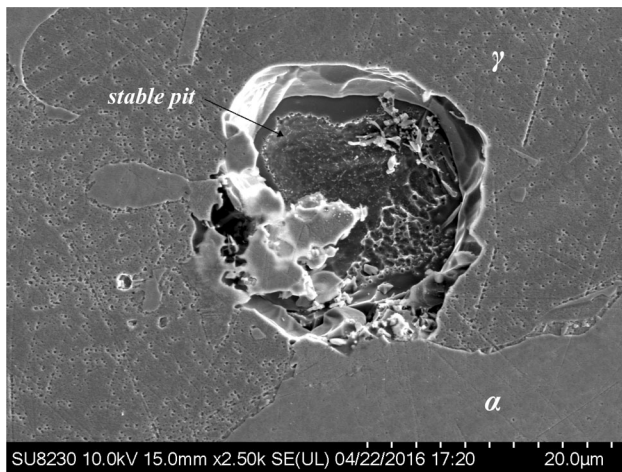
Fig. 14—SE-SEM image showing the pit located at the ferrite/austenite boundary in sample aged at 973 K (700 °C) for 24 h.
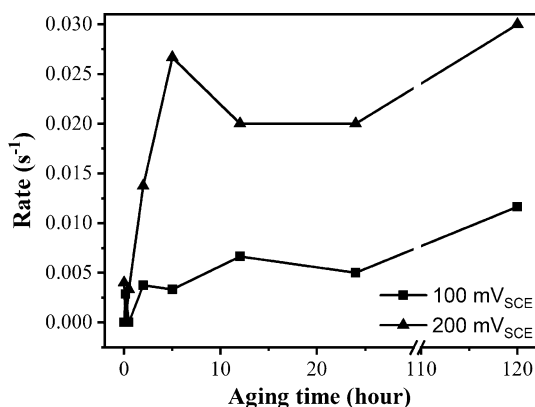


Fig. 15—Change in the rate of metastable pitting in the potential range of 0 through 100 mV$_{SCE}$ and 100 through 200 mV$_{SCE}$ with aging time.
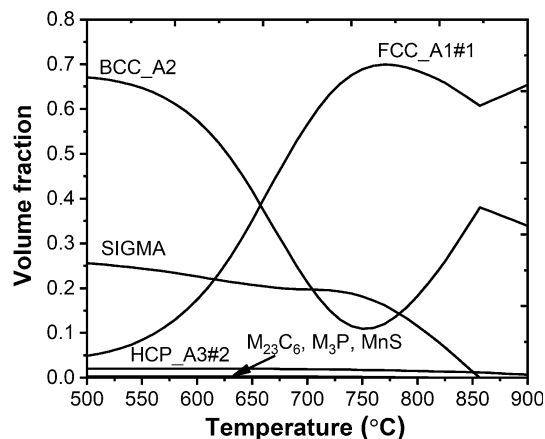


Fig. 16—Thermo-Calc prediction of stable phases within the temperature range of 773 K to 1173 K (500 °C to 900 °C). BCC_A2: the ferrite phase; FCC_A1#1: the austenite phase; SIGMA: σ phase; HCP_A3#2: nitride.

850 °C).[13,21,24,26] Since the intermetallic phases are enriched in Cr and Mo, the lower Cr and Mo content in UNS S32003 leads to the slow formation of intermetallic phases. In addition, Cr-depletion was found in the vicinity of nitride precipitates in samples aged at 1073 K (800 °C), but not detected next to the precipitates in samples aged at 1173 K (900 °C), as shown in Figures 6 and 7. The kinetics of nitride precipitation is slower compared with that at 1073 K (800 °C). Also, the diffusion rate is faster at higher temperature at 1173 K (900 °C), leading to a fast Cr replenishment next to nitride precipitates. Both factors contribute to the absence of Cr-depleted zone or a low extent of Cr depletion that's below the detecting limit of EDS analysis in samples aged at 1173 K (900 °C).

However, σ phase was detected after a long-term aging (120 hours) at 973 K (700 °C) for in UNS S32003. Thermodynamic predication through Thermo-Calc indicates that σ phase is stable phase within temperature range of 773 K to 1127 K (500 °C to 854 °C), as shown in Figure 16. Although M$_3$P, M$_{23}$C$_6$ and MnS are also predicted to be stable within this temperature range, however, their volume fraction was in the order of $10^{-5}$

to $10^{-3}$ and they were not detected in all aged samples using SEM/EDS technique. This is probably because of the low content of element P, C and S in this alloy. M$_{23}$C$_6$ has been observed to precipitate along with Cr$_2$N using electron backscatter diffraction (EBSD) technique,[15] however, it is not possible to quantify M$_{23}$C$_6$ using SEM/EDS analysis because of the unavoidable carbon contamination in the SEM chamber. Although it has been reported that χ phase precipitated together with σ phase,[26,27] it was not observed in the present study. Both χ phase and σ phase are enriched in Cr and Mo, however, χ phase has high Mo content more than 10 wt pct.[8,10,26,27] Table IV shows the chemical compositions of different phases in samples aged at 973 K (700 °C) for 120 hours, and the Mo content is 4.6 wt pct with 95 pct confidence interval of 0.4 wt pct, indicating that only σ phase is present after aging at 973 K (700 °C) for 120 hours. This may be because the χ phase is a metastable phase and after 120 hours of aging, it might have already transformed into σ phase.[27]

As shown in Figures 10 and 11, phase transformation process during isothermal aging at 973 K (700 °C) in UNS S32003 involves first precipitation of nitrides and possibly carbides, and then the precipitation of σ phase after longer aging time. As shown in Figure 10(c), σ phase formed within the ferrite phase or along the ferrite/austenite boundaries and propagated into the ferrite phase, because of the higher diffusion rate and higher content of Cr and Mo in the ferrite phase. This process is similar to what has been observed in the lean duplex stainless steel UNS S32101 during isothermal aging at 963 K (690 °C), where the σ phase was found to precipitate in the vicinity of nitride and carbide precipitates because of the local changes in the element content.[15]

## B. Effects of Aging on Pitting Corrosion Behavior

Results in Figure 8 compare the pitting potential of samples aged at different temperatures for 30 minutes and 2 hours. Staring from 923 K (650 °C) aged samples, the pitting potential first dropped with an increase in the

aging temperature reaching a lowest value around 1073 K to 1123 K (800 °C to 850 °C), and then the pitting potential increased for the samples aged at 1173 K (900 °C). This is consistent with the microstructural evolution where for the samples aged at 1073 K (800 °C), the volume fraction of precipitates is the highest and the Cr-depleted zones is present, as shown in Figure 4. With the longer aging times at 973 K (700 °C), there is a decrease in the pitting potential as well as the repassivation potential, as shown in Figure 13. An increased metastable pitting rate was also observed with longer aging times, indicating the deteriorating effect of aging on pitting corrosion resistance, as shown in Figure 15.

Figures 9 and 14 showed that the pit initiation sites reside at the ferrite/austenite boundary and close to the nitride precipitates. It is evident in Figure 9 that the pit initiation is closely related to the precipitate formation, probably because of the Cr-depleted zones associated with the precipitates. Since Cr is a major element in the passive film and is responsible for an increased corrosion resistance of stainless steels, the depletion of Cr in the vicinity of precipitates and $\sigma$ phase seems to be the major reason for the deterioration of pitting corrosion resistance of aged samples. Except for the sample aged at 973 K (700 °C) for 120 hours which also had $\sigma$ phase precipitates, all aged samples had nitride precipitates, and the volume fraction of precipitates was below 1 pct. However, the change in the pitting corrosion resistance in terms of pitting potential, repassivation potential and metastable pitting event rates is very sensitive to the variation in the fraction of precipitates.

## V. CONCLUSIONS

1. Only nitrides precipitates were positively detected along the ferrite/austenite phase boundaries and within the ferrite phase for the UNS S32003 samples aged in the temperature range of 873 K to 1173 K (600 °C to 900 °C) for up to 2 hours.
2. The precipitation kinetics was the fastest at 1073 K (800 °C) for the UNS S32003, where the Cr-depleted zones were observed to be in the vicinity of the precipitates.
3. For samples aged at 973 K (700 °C) for 120 hours, $\sigma$ phase was detected along with an increase in the percentage of precipitates.
4. Precipitates were found to be at the edge of small pits, indicating the pit initiation is close to the precipitates and is probably associated with the Cr-depleted zones.
5. Pitting corrosion resistance decreased with higher fraction of nitride precipitates and the formation of $\sigma$ phase. The change in the pitting corrosion resistance in terms of pitting potential, repassivation potential and metastable pitting rate is very sensitive to the precipitation of secondary phases even when the volume fraction of these precipitates is below 1 pct.

## REFERENCES

1. A. Bhattacharya and P.M. Singh: *J. Fail. Anal. Prev.*, 2007, vol. 7, pp. 371–77.
2. V. Muthupandi, P. Bala Srinivasan, S.K. Seshadri S. Sundaresan: *Mater. Sci. Eng. A*, 2003, vol. 358, pp. 9–16.
3. R. Badji, M. Bouabdallah, B. Bacroix, C. Kahloun, B. Belkessa, and H. Maza: *Mater. Charact.*, 2008, vol. 59, pp. 447–53.
4. Leif: *Welding World*, 2012, vol. 56, pp. 65–76.
5. L. Zhang, W. Zhang, Y. Jiang, B. Deng, D. Sun, and J. Li: *Electrochim. Acta*, 2009, vol. 54, pp. 5387–92.
6. Y. Yang, H. Tan, Z. Zhang, Z. Wang, Y. Jiang, L. Jiang, and J. Li: *CORROSION*, 2012, vol. 69, pp. 167–73.
7. L. He and P.M. Singh, In *CORROSION 2017*, (NACE International: New Orleans, Louisiana, USA, 2017), p 8.
8. D.C. dos Santos and R. Magnabosco: *Metall. Mater. Trans. A*, 2016, vol. 47A, pp. 1554–65.
9. J. Michalska and M. Sozańska: *Mater. Charact.*, 2006, vol. 56, pp. 355–62.
10. I. Calliari, M. Pellizzari, M. Zanellato, and E. Ramous: *J. Mater. Sci.*, 2011, vol. 46, p. 6916.
11. H. Sieurin and R. Sandström: *Mater. Sci. Eng. A*, 2007, vol. 444, pp. 271–76.
12. A. Bhattacharya and P.M. Singh: *Metall. Mater. Trans. A*, 2009, vol. 40A, pp. 1388–99.
13. M.E. Wilms, V.J. Gadgil, J.M. Krougman, and F.P. Ijsseling: *Corros. Sci.*, 1994, vol. 36, pp. 871–81.
14. C.J. Park, V.S. Rao, and H.S. Kwon: *Corrosion*, 2005, vol. 61, pp. 76–83.
15. J.-Y. Maetz, S. Cazottes, C. Verdu, and X. Kleber: *Metall. Mater. Trans. A*, 2016, vol. 47A, pp. 239–53.
16. M. Naghizadeh and M.H. Moayed: *Corros. Sci.*, 2015, vol. 94, pp. 179–89.
17. Z. Wei, J. Laizhu, H. Jincheng, and S. Hongmei: *Mater. Charact.*, 2009, vol. 60, pp. 50–55.
18. Z. Zhang, H. Zhao, H. Zhang, Z. Yu, J. Hu, L. He, and J. Li: *Corros. Sci.*, 2015, vol. 93, pp. 120–25.
19. L. Zhang, Y. Jiang, B. Deng, W. Zhang, J. Xu, and J. Li: *Mater. Charact.*, 2009, vol. 60, pp. 1522–28.
20. K. Ravindranath and S.N. Malhotra: *Corros. Sci.*, 1995, vol. 37, pp. 121–32.
21. B. Deng, Z. Wang, Y. Jiang, T. Sun, J. Xu, and J. Li: *Corrosion Science*, 2009, vol. 51, pp. 2969–75.
22. B. Deng, Z. Wang, Y. Jiang, H. Wang, J. Gao, and J. Li: *Electrochim. Acta*, 2009, vol. 54, pp. 2790–94.
23. A. Bhattacharya and P.M. Singh: *Corrosion*, 2008, vol. 64, pp. 532–40.
24. L. Pezzato, M. Lago, K. Brunelli, M. Breda, and I. Calliari: *J. Mater. Eng. Perform.*, 2018, vol. 27, pp. 3859–68.
25. I. Calliari, M. Dabalà, E. Ramous, and G. Straffelini: *Mater. Sci. Forum*, 2009, vols. 604–605, pp. 419–26.
26. T.H. Chen, K.L. Weng, and J.R. Yang: *Mater. Sci. Eng. A*, 2002, vol. 338, pp. 259–70.
27. E.A. Melo and R. Magnabosco: *Metall. Mater. Trans. A*, 2017, vol. 48A, pp. 5273–84.